Journal of
Materials Chemistry A

Materials for energy and sustainability

ROYAL SOCIETY
OF **CHEMISTRY**

PAPER
Feng Gao, Hongliang Du, Li Jin *et al.*
Enhancing energy storage performance in
$Na_{0.5}Bi_{0.5}TiO_3$-based lead-free relaxor ferroelectric
ceramics along a stepwise optimization route

10 YEARS
ANNIVERSARY

PAPER

Check for updates

Enhancing energy storage performance in Na$_{0.5}$Bi$_{0.5}$TiO$_3$-based lead-free relaxor ferroelectric ceramics along a stepwise optimization route†

Wen Wang,[a] Leiyang Zhang, [iD] [a] Yule Yang,[a] Wenjing Shi,[a] Yunyao Huang,[a] D. O. Alikin,[b] V. Ya. Shur,[b] Zhihao Lou,[c] Amei Zhang,[d] Xiaoyong Wei, [iD] [a] Dong Wang,[e] Feng Gao, [iD] *[c] Hongliang Du [iD] *[d] and Li Jin [iD] *[a]

Despite the fact that relaxor ferroelectrics (RFEs) have been extensively researched because of their various advantages, there are still barriers to simultaneously increasing their energy storage density (W_{rec}) and efficiency (η). By substituting Bi(Mg$_{0.5}$Sn$_{0.5}$)O$_3$ (BMS) and optimizing the formation process, this study follows a stepwise optimization route to achieve comprehensive exceptional energy storage performance (ESP) in Na$_{0.5}$Bi$_{0.5}$TiO$_3$-Sr$_{0.85}$Bi$_{0.1}$TiO$_3$ (NBT-SBT)-based ceramics. On the premise of constructing a Sr^{2+}–Sr^{2+} ion pair at the A-site to ensure a large polarization, the introduction of Mg^{2+} and Sn^{4+} ions at the B-site further induces a local disordered field and promotes polar nanoregions. Following that, the viscous polymer process (VPP) used to synthesize NBT-SBT-BMS ceramics can thin the thickness, reduce defects, and boost compactness, hence improving the polarization difference (ΔP) and breakdown strength (E_b). Using the stepwise optimization route, we were able to attain a high ΔP of 64.6 μC cm^{-2} and an E_b of 440 kV cm^{-1} in 0.92(0.65NBT-0.35SBT)-0.08BMS-VPP ceramics. More crucially, an ultrahigh W_{rec} of 7.5 J cm^{-3} and a high η of 85% are simultaneously achieved, together with excellent temperature adaptability between 20 and 120 °C. Our superb ESP exceeds the majority of previously reported NBT-based ceramics, confirming the applicability of this stepwise optimization route to other similar high-performance dielectric ceramic designs.

1. Introduction

Ceramic dielectric capacitors are capably competitive in electronic systems because of their high-power density, strong voltage resistance, and prominent reliability.[1–3] Their poor energy storage density, however, remains an impediment to meeting the demands for advanced electronic system integration and downsizing.[4,5] To compensate for this shortcoming, reduce energy loss, and adapt to diverse temperature conditions, ceramic capacitors with high energy storage density (W_{rec}), energy efficiency (η), and great thermal adaptation are required.[1] The desirable W_{rec} and η are theoretically fulfilled by high breakdown strength (E_b) and large polarization difference (ΔP) between maximum polarization (P_m) and residual polarization (P_r), based on polarization against electric field (P–E) hysteresis loops of ceramics.[6] In this regard, relaxor ferroelectrics (RFEs) have a high ΔP value and a moderate E_b, giving them advantages and superiorities over ferroelectrics (FEs), antiferroelectrics (AFEs), and linear dielectrics (LDs), all of which have advantages and disadvantages in energy storage applications.[3]

Perovskite (Na$_{0.5}$Bi$_{0.5}$)TiO$_3$ (NBT)-based RFE ceramics have been extensively studied in the past decade.[4,5,7–15] Because the valence electron configuration of Bi^{3+} (6s^{2}6p^0) is comparable to that of Pb^{2+} and orbital hybridization between Bi 6p and O 2p normally generates a higher P_m, prototypical NBT has a high P_m greater than 40 μC cm^{-2}.[1] Nonetheless, its high P_r (38 μC cm^{-2}) and relative square P–E loop are detrimental to W_{rec} improvement. Based on this, one of the effective modification strategies for improving the energy storage performance (ESP) of NBT-based ceramics is chemical modification by substituting (Sr$_{0.85}$Bi$_{0.1}$)TiO$_3$ (SBT) into NBT.[7,16] The total strength of the electrostatic bond of all adjacent cations to an anion is equal to

Electronic Materials Research Laboratory, Key Laboratory of the Ministry of Education, School of Electronic Science and Engineering, Xi'an Jiaotong University, Xi'an, 710049, China. E-mail: ljin@mail.xjtu.edu.cn

School of Natural Sciences and Mathematics, Ural Federal University, Ekaterinburg, 620000, Russia

State Key Laboratory of Solidification Processing, MIIT Key Laboratory of Radiation Detection Materials and Devices, USI Institute of Intelligence Materials and Structure, School of Materials Science and Engineering, Northwestern Polytechnical University, Xi'an 710072, China. E-mail: gaofeng@nwpu.edu.cn

Multifunctional Electronic Ceramics Laboratory, College of Engineering, Xi'an International University, Xi'an 710077, China. E-mail: duhongliang@126.com

Frontier Institute of Science and Technology and State Key Laboratory for Mechanical Behaviour of Materials, Xi'an Jiaotong University, Xi'an 710049, China

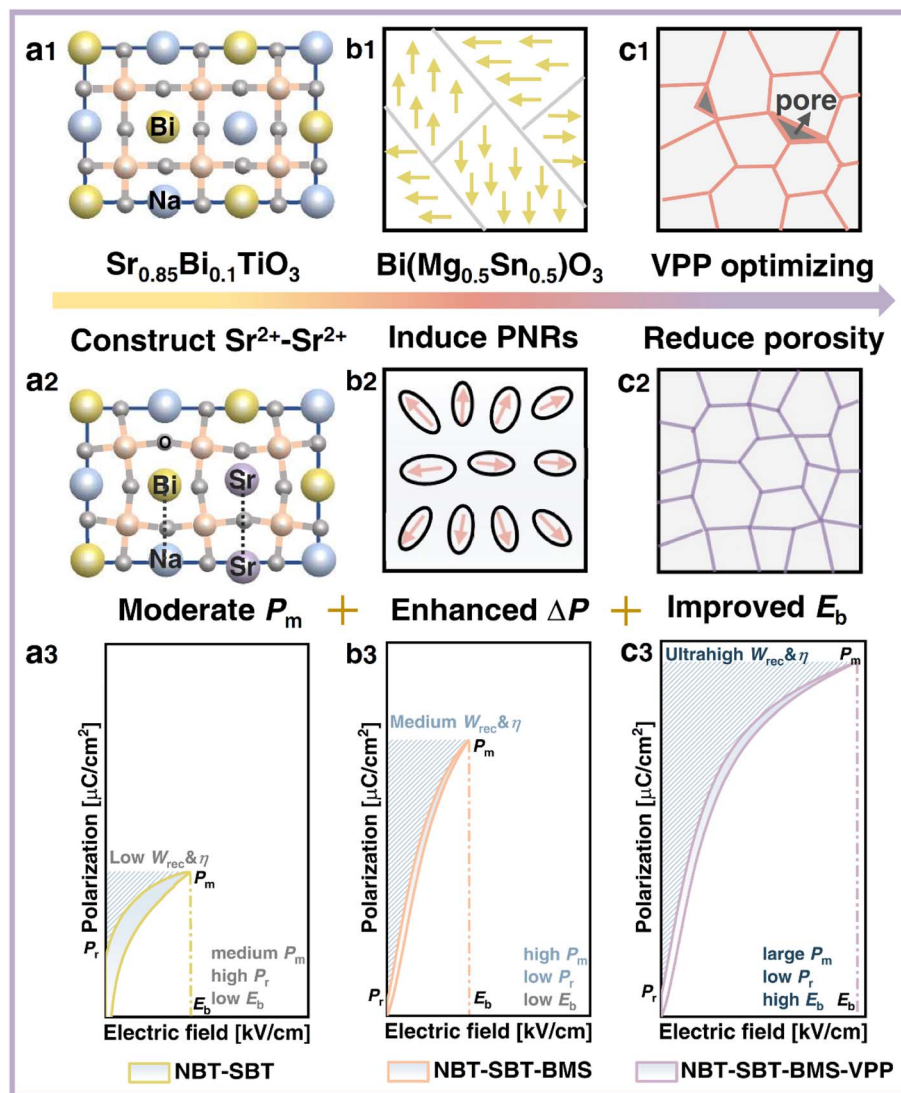† Electronic supplementary information (ESI) available. See DOI: https://doi.org/10.1039/d2ta09395b

Fig. 1 Schematic diagram of a stepwise optimization route to enhance energy storage characteristics *via* (a1–a2) ion pairs construction, (b1–b2) domain engineering and (c1–c2) process optimization for NBT-based ceramics. (a3–c3) Schematic diagram of $P–E$ loops for realizing improved energy storage properties.

the anion's charge, according to the electrostatic valency principle. As a result, adjacently formed Sr^{2+}–Sr^{2+} can replace Bi^{+}–Na^{3+} in the NBT-SBT system, as shown in Fig. 1(a1 and a2). Combined with Coulomb's law $F = kq_1q_2/r^2$, the distance of the former with $q = +2_{Sr}$ is greater than that of the latter with $q = +1_{Na}$ and $q = +3_{Bi}$. Following that, such a replacement is built by introducing SBT into NBT to cause A-position asymmetry, larger atomic space, and lattice distortion, resulting in a moderate P_m. Furthermore, due to its dielectric relaxation behavior over a wide temperature range, SBT can help to improve the thermal stability of ceramics.[7] In this case, NBT-SBT is chosen as the matrix for this work due to its high P_m and potential temperature characteristics, while its nonnegligible P_r and low E_b limit the ultimate excellent ESP, as depicted in Fig. 1(a3).

As a result, many studies have been conducted to improve the above two points of the NBT-SBT system by introducing niobate compounds such as $NaNbO_3$ (NN),[16] $KNbO_3$,[17] $AgNbO_3$

(AN),[18,19] and $(Na, K)NbO_3$ (KNN) in this matrix.[8] For example, Wu *et al.* acquired an enhanced W_{rec} of 3.08 J cm^{-3} by incorporating NN into NBT-SBT systems with an increased E_b of 220 kV cm^{-1}.[16] Furthermore, $BiMeO_3$ compounds (Me representing various cations) are frequently substituted into NBT-based systems to improve relaxation behavior and E_b, which are attributed to the strong polarizability of Bi^{3+} and the reduced grain size by large radius Me^{3+} ions.[20,21] As a result, $Bi(Mg_{0.5}$-$Sn_{0.5})O_3$ (BMS), which has the potential to decrease P_r while increasing E_b, is chosen as the first optimization route, as shown in Fig. 1(b1 and b2). The difference in charge and ionic radius in the B-site induces a local disordered field, which contributes to the realization of the transition from microdomains to polar nanoregions (PNRs) that respond quickly to an applied electric field, thus maintaining a large ΔP and improving E_b, as shown in Fig. 1(b3).

2642 | *J. Mater. Chem. A*, 2023, **11**, 2641–2651

This journal is © The Royal Society of Chemistry 2023

In addition, the E_b is affected by other factors such as thickness, grain size, porosity, and so on, so many measures to improve the E_b have been implemented around these factors.[22] Li et al., for example, achieved an increased E_b of 600 kV cm^{-1} in $K_{0.5}Na_{0.5}NbO_3$-$Bi(Zn_{2/3}Ta_{1/3})O_3$ ceramics by reducing thickness and porosity through repeated rolling.[23] Yan et al. also achieved a high E_b of 500 kV cm^{-1} in $Bi_{0.5}Na_{0.5}TiO_3$-$SrNb_{0.5}Al_{0.5}O_3$ ceramics using the tape casting technique.[24] As a result, the viscous polymer process (VPP)[25,26] is used in the second optimization route to increase the E_b of NBT-SBT-BMS ceramics, as shown in Fig. 1(c1 and c2). The NBT-SBT-BMS ceramic powders are treated with PVA, hot water, acetic acid, and repeated rolling to obtain thinner, less defective, and denser VPP ceramics, which ultimately helps to obtain higher E_b and improve ESP, as indicated in Fig. 1(c3).

Along the stepwise optimization route depicted in Fig. 1. NBT-SBT-BMS-VPP ceramics are synthesized by introducing BMS and optimizing the VPP process in the NBT-SBT matrix with the formation of Sr^{2+}–Sr^{2+} ion pairs, which improve P_m, reduce P_r and finally improve E_b. In summary, the 0.92(0.65NBT-0.35SBT)-0.08BMS-VPP ceramics optimized by this progressive strategy achieve an ultrahigh W_{rec} of 7.5 J cm^{-3} and a high η of 85% at a large ΔP of 64.6 μC cm^{-2} (E_b = 440 kV cm^{-1}), as well as excellent temperature applicability within 20–120 °C.

2. Experimental

$(1-x)(0.65Na_{0.5}Bi_{0.5}TiO_3$-$0.35Sr_{0.85}Bi_{0.1}TiO_3)$-$xBi(Mg_{0.5}Sn_{0.5})O_3$ ceramics (abbreviated as NBT-SBT-xBMS, x = 0.02, 0.04, 0.08, and 0.12) were first prepared using the solid-state reaction method, and then the x = 0.08 component was optimized using the VPP process. ESI† contains information on the experimental procedure and characterization.

3. Results and discussion

The crystalline structure detected by XRD for NBT-SBT-xBMS ceramics is shown in Fig. 2(a), all of which are solid soluble perovskite structures except for the second phase caused by Bi
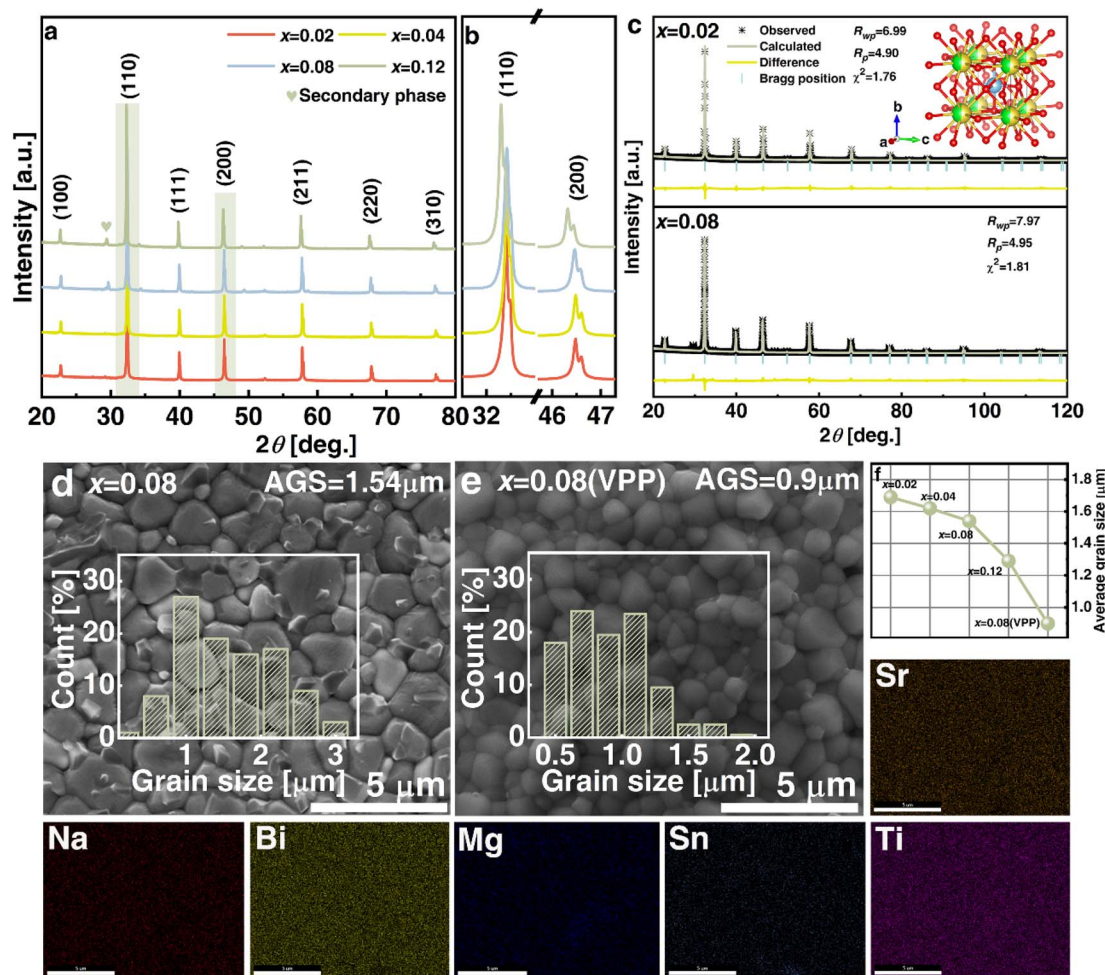

Fig. 2 XRD patterns of NBT–SBT-xBMS ceramics (a) in the range 20–80° and (b) the enlarged XRD profiles of the (110) and (200) peaks. (c) Rietveld refinements for x = 0.02 and x = 0.08 ceramics. The SEM micrographs of (d) x = 0.08 and (e) x = 0.08 (VPP) ceramics. The insets are average grain size distributions. (f) The average grain size (AGS) of NBT–SBT-xBMS ceramics. (Sr–Ti) The energy-dispersive X-ray spectroscopy (EDS) mapping images of x = 0.08 ceramics.

This journal is © The Royal Society of Chemistry 2023

J. Mater. Chem. A, 2023, **11**, 2641–2651 | **2643**

volatilization during the high-temperature process and labeled at 28–29°. The enlarged (110) peaks in Fig. 2(b) shift to the left as BMS content increases, as does cell volume, because bigger radius Mg^{2+} (72 pm) and Sn^{4+} (69 pm) ions replace Ti^{4+} ions (60.5 pm). Similarly, the cleaved (200) peaks show that ceramics are not cubic in structure but have pseudocubic symmetry, as determined by the Rietveld refinements of all compositions in Table S1† and Fig. 2(c). The average structures are $Pm\bar{3}m$, according to the fitting R-factors in the refinement results, and the changes in lattice parameters and cell volume are consistent with the XRD analyses. Furthermore, Fig. 2(d) and (e) compare the SEM micro appearances and average grain size (AGS) distributions of $x = 0.08$ and $x = 0.08$ (VPP) ceramics, with the

latter being denser than the former due to the reduced porosity achieved through VPP processing. Fig. 2(f) shows the AGS distribution results of each ceramic component, with the AGS steadily decreasing from 1.69, 1.62, 1.54, 1.29 to 0.9 μm with the addition of BMS and VPP. The element distributions (EDS) of the optimal VPP object ($x = 0.08$) are then shown in Fig. 2(Sr–Ti), exhibiting the chemical uniformity of the elements Sr, Na, Bi, Mg, Sn, and Ti. As is generally known, grain size, porosity, and compactness are all parameters that can influence the E_b of ceramics by varying the quantity of high-insulating grain boundaries.[2,22] As a result, the E_b of NBT-SBT-xBMS ceramics is evaluated in terms of the Weibull distribution, as illustrated in Fig. 3(a), where all data obey the distribution and fit out the
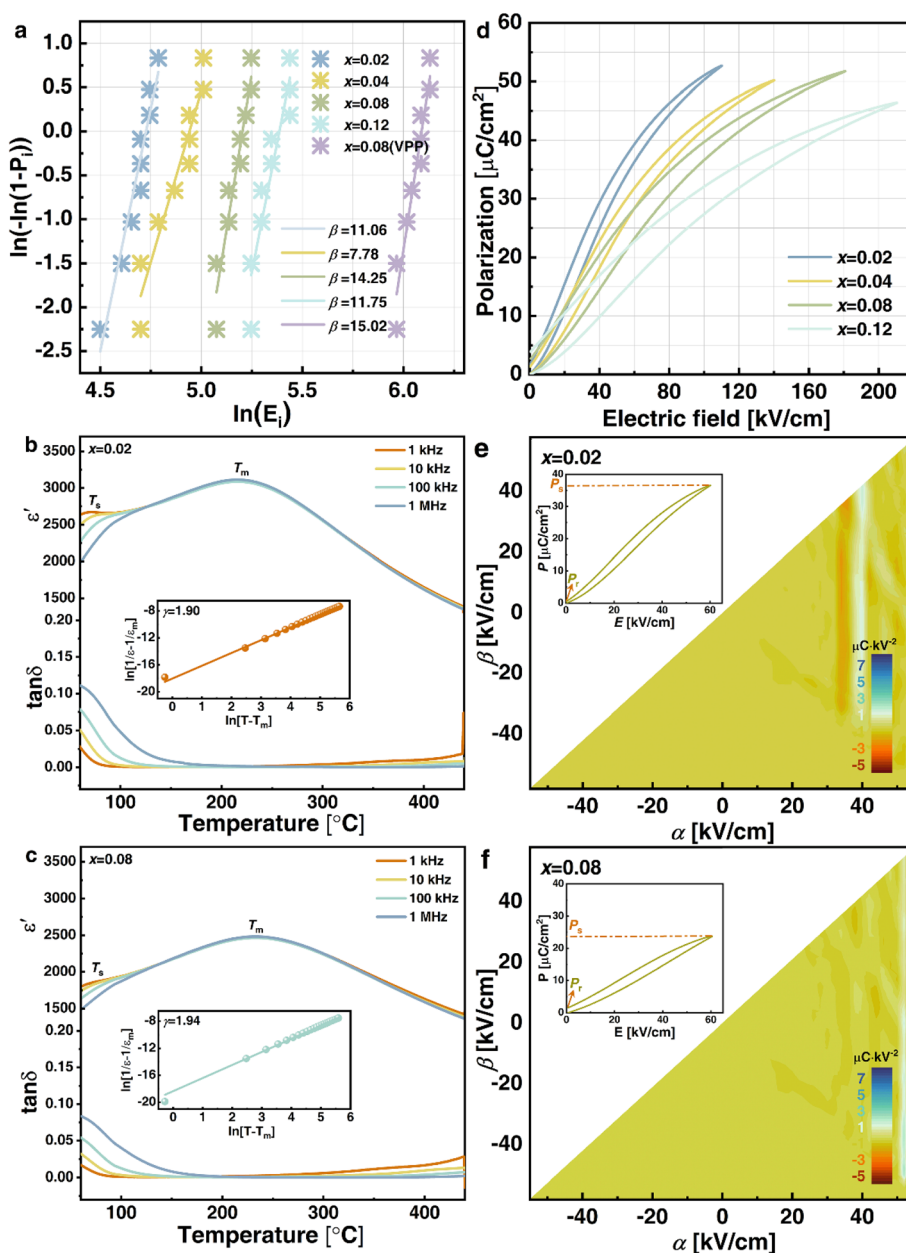

Fig. 3 (a) Weibull distributions of NBT–SBT–xBMS ceramics. Temperature dependent permittivity (ε') and loss tangent (tan δ) at 1–1000 kHz of (b) $x = 0.02$ and (c) $x = 0.08$ ceramics. The insets are $\ln(1/\varepsilon' - 1/\varepsilon_{max})$ versus $\ln(T - T_{max})$. (d) Unipolar P–E loops under the critical electric field of NBT–SBT–xBMS ceramics. Evolution of the FORC distribution of (e) $x = 0.02$ and (f) $x = 0.08$ ceramics.

2644 | J. Mater. Chem. A, 2023, **11**, 2641–2651

This journal is © The Royal Society of Chemistry 2023

reliable value β. The increasing E_b is inversely proportional to the decreasing AGS, which conforms to the relationship between them, *i.e.*, $E_b \propto 1/\sqrt{G}$, where G represents the AGS.[22]

Fig. 3(b) and (c) show the temperature dependences of dielectric properties for $x = 0.02$ and 0.08 ceramics. The noticeable frequency dispersion at a low temperature of about 60 °C in the loss tangent $(\tan \delta) - T$ curves of these two ceramics can be detected as the one dielectric anomaly (T_s peak) in the corresponding permittivity $(\varepsilon') - T$ spectrum, which is created by the thermal evolution of PNRs.[27,28] In contrast, another dielectric anomaly (T_m peak) corresponding to maximum permittivity ε_m exists in the high-temperature area of 250 °C due to the weak frequency dispersion. After doping additional BMS, the ε' of $x = 0.08$ ceramics dramatically falls compared to $x = 0.02$ and 0.08 ceramics due to increasing cation disorder at A- and B-sites as well as the broken long-range ferroelectric order. Furthermore, the dielectric peak of $x = 0.08$ ceramics becomes wide and flat, which improves relaxor behavior, increases the thermal stable interval, and contributes to ESP temperature stability. In order to determine the diffuseness degree of $x = 0.02$ and 0.08 ceramics further, the modified Curie–Weiss law is used as follows:[29]

$$\frac{1}{\varepsilon'} - \frac{1}{\varepsilon_m} = \frac{(T - T_m)^\gamma}{C}, \qquad (1)$$

where C and γ are the Curie constant and diffusion coefficient, respectively. The $\ln(1/\varepsilon' - 1/\varepsilon_m) - \ln(T - T_m)$ curves of $x = 0.02$ and 0.08 ceramics are respectively plotted and fitted in the insets of Fig. 3(b) and (c). When x changes from 0.02 to 0.08, the γ values increase from 1.90 to 1.94. As a result, the $x = 0.08$

ceramic has a greater diffuse state, which can be attributed to cation confusion, FE long-range breaking, and the effects of PNRs.[30,31] Fig. 3(d) depicts the unipolar P–E loops of NBT-SBT-xBMS ceramics under critical electric fields. When the amount of BMS dopants varies from 0.02 to 0.12, the P–E loops become flat and fat, accompanied by an increase in P_r. Despite the fact that the P_m of all compositions falls when subjected to the same electric field, the P_m can also be maintained at high electric fields produced by increasing BMS concentrations. Meanwhile, for $x = 0.02$, 0.04, 0.08, and 0.12, the E_b is 110, 140, 180, and 210 kV cm^{-1}, respectively. The first-order reversal curves (FORCs) of $x = 0.02$ and $x = 0.08$ ceramics under 60 kV cm^{-1} are executed in Fig. 3(e) and (f), separately. The high concentration region of $x = 0.02$ ceramic exhibits a significant nonlinear polarization behavior, based on the different polarization intensity and behavior reflected by the background shade.[32] As a result, the increased P_m in the inset curves is generated by domain flipping and domain wall motion driven by ferroelectric behavior. In the case of $x = 0.08$ ceramic, the high-strength region near the origin becomes more dispersed, and the area of long-range polarization order gradually declines, implying that the ferroelectricity is weakened, the long-range FE order is broken, and relaxor behaviour is enhanced.

Bright-field transmission electron microscopy (TEM) examination is performed to observe the domain morphology in order to better investigate the physical mechanism of the remarkable ESP in the optimal $x = 0.08$ ceramic, as shown in Fig. 4(a). Because of the introduction of BMS, micron-sized PNRs have clearly replaced huge ferroelectric domains in ceramics. The lattice spacing confirms the average structure of pseudocubic
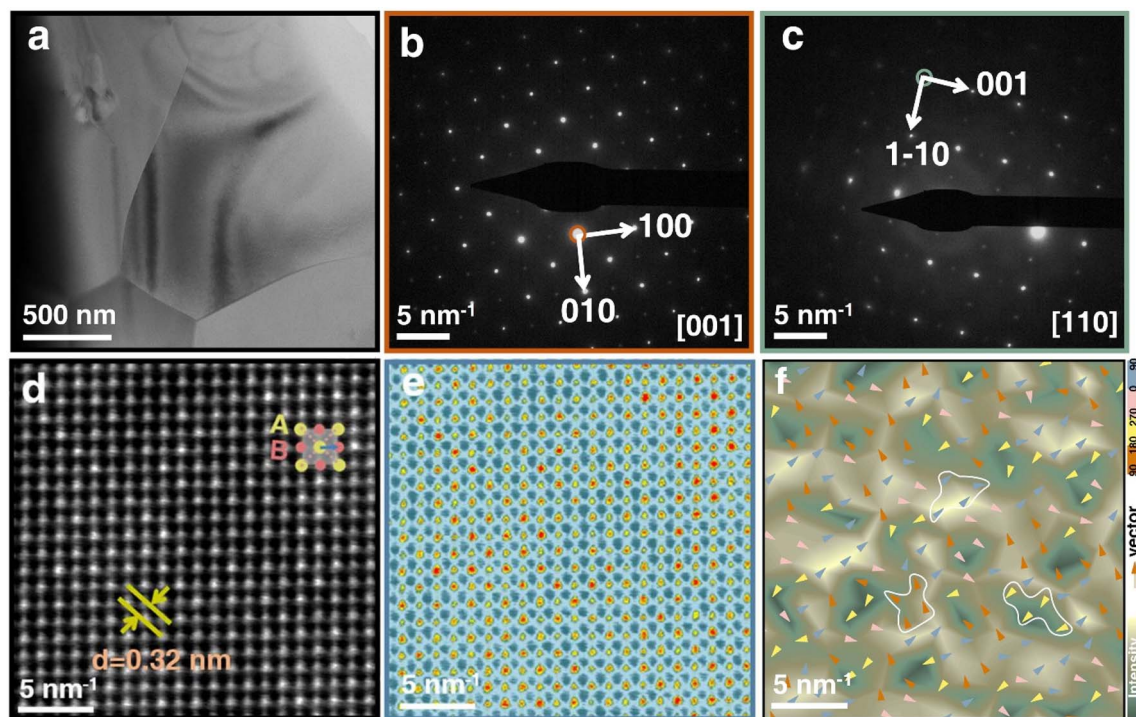

Fig. 4 TEM images of $x = 0.08$ ceramics: (a) bright-field, SAED patterns along (b) [001]$_C$ and (c) [110]$_C$, (d) HR-TEM images, (e) atomic brightness contrast extracted from (d), and (f) the spontaneous polarization vectors calculated from the displacement of the B-site cations.

This journal is © The Royal Society of Chemistry 2023

J. Mater. Chem. A, 2023, **11**, 2641–2651 | **2645**

symmetry, according to the selected-area electron diffraction (SAED) patterns along the [001] and [110] zone axes of the $x = 0.08$ ceramic grains shown in Fig. 4(b) and (c), which is consistent with the XRD refinement results. The high-resolution TEM (HR-TEM) images in Fig. 4(d) and concomitant brightness distribution in Fig. 4(e) of the $x = 0.08$ ceramic jointly point out the A- and B-sites atom positions. As a result, the spontaneous polarization vector is identified as the distance from the cationic B-site to the nearest four A-site centers. Based on this assumption, Fig. 4(f) depicts the intensity and orientation of spontaneous polarization, as shown by the back color distribution and arrow direction, respectively. Meanwhile, four-angle interval arrow vectors (0-90-180-270-360°) divided into four colors correspond to different back color regions showing polarization intensity. PNRs are regions (indicated by a white line) composed of polarization vectors of the same color and orientation, where the (2–4) nm PNRs and domain structure in the $x = 0.08$ ceramic are helpful for improving ΔP and ESP.

Fig. 5(a–c) show the unipolar P–E loops and relative I–E curves of $x = 0.02$, 0.08, and 0.08 (VPP) ceramics under various electric fields. Because of the comparatively obvious hysteresis embedded in the P–E loops, the $x = 0.02$ ceramics in Fig. 5(a) exhibit weak RFE features, with low E_b as well as significant P_m

and P_r values. Under the same electric field, P_m falls and P_r increases after the addition of 0.08 mole BMS in Fig. 5(b) compared to $x = 0.02$. Despite this, BMS has greatly improved the E_b of $x = 0.08$ to give a P_m value that is still high under this breakdown field. As a result, $x = 0.08$ is determined for further VPP to synthesize $x = 0.08$ (VPP) ceramics in Fig. 5(c), which intuitively have slimmer P–E loops. The VPP reduces thickness, flaws, and porosity, resulting in greatly higher E_b, equally high P_m, and significantly reduced P_r. The foregoing trends of $x = 0.02$, 0.08, and 0.08 (VPP) ceramics are independently reflected in the specific performance parameters (E_b, P_m, P_r, W_{rec}, and η) observed under different electric fields in Fig. 5(d–f). With a low E_b of 110 kV cm^{-1} for $x = 0.02$ ceramics in Fig. 5(d), the large P_m of 52.68 μC cm^{-2} and P_r of 1.66 μC cm^{-2} result in an undesired ESP ($W_{rec} = 2.1$ J cm^{-3}, $\eta = 87\%$). Then under the function of BMS for $x = 0.08$ ceramics in Fig. 5(e), the enhanced E_b (180 kV cm^{-1}) boosts the modified W_{rec} (3.2 J cm^{-3}) but the increased P_r (2.65 μC cm^{-2}) cause a reduced η of 85%. The ESP has yet to meet the actual application requirements. As a result, the ESP of $x = 0.08$ ceramics is naturally enhanced by VPP, achieving ultrahigh W_{rec} of 7.5 J cm^{-3} and η of 85% under E_b of 440 kV cm^{-1} as shown in Fig. 5(f). Fig. 5(g) depicts the effects of key parameters such as E_b and $P_m - P_r$ on W_{rec} for the three
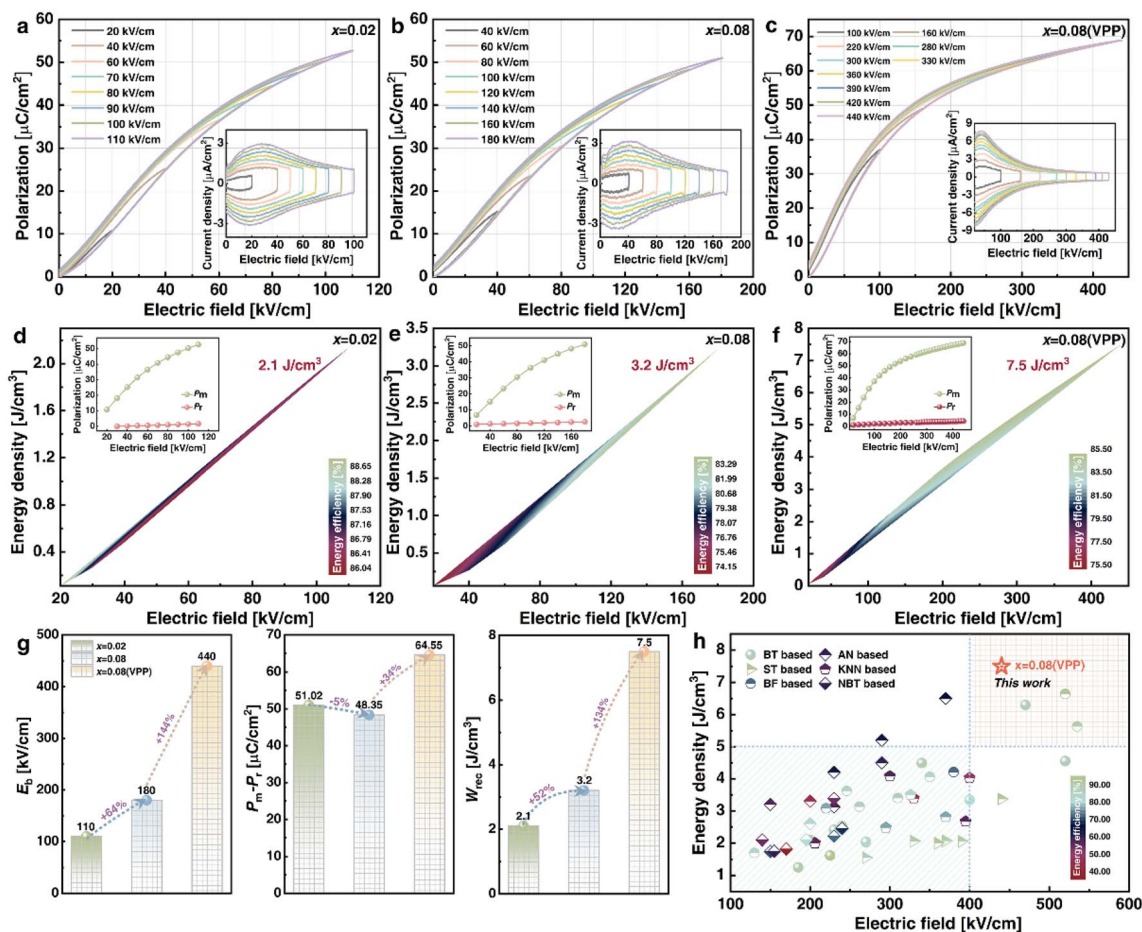

Fig. 5 (a–c) Unipolar P–E loops, (d–f) the calculated W_{rec} and η of at different electric fields for $x = 0.02$, $x = 0.08$ and $x = 0.08$ (VPP) ceramics. (g) Comparison of E_b, $P_m - P_r$ and W_{rec} values among $x = 0.02$, $x = 0.08$ and $x = 0.08$ (VPP) ceramics. (h) Comparison of W_{rec}, η and E_b between this work and other reported lead-free ceramics.

2646 | *J. Mater. Chem. A*, 2023, **11**, 2641–2651

This journal is © The Royal Society of Chemistry 2023

ceramics. As 0.08 mol. BMS and VPP act sequentially to improve E_b from 110 kV cm^{-1} by 64% to 180 kV cm^{-1} and subsequently by 144% to 440 kV cm^{-1}, the ΔP decreases by 5% from 51.02 μC cm^{-2} to 64.55 μC cm^{-2}. As a result, the massive increase in W_{rec} from 2.1 to 7.5 J cm^{-3} is ultimately realized in $x = 0.08$ (VPP) ceramics, which is primarily attributed to the overall improved E_b and ΔP. In addition, a succession of E_b, W_{rec}, and η between our work and BaTiO$_3$ (BT), AN, SrTiO$_3$ (ST), KNN, BiFeO$_3$ (BF), and NBT-based ceramics are shown in Fig. 5(h).[10,15,16,18,22,33–77]

Most ceramic performance parameters are spread in the lower left and upper right corners of each system, with E_b below 400 kV cm^{-1} linearly corresponding to W_{rec} below 5 J cm^{-3} and *vice versa*. However, the $x = 0.08$ (VPP) ceramic with W_{rec} of 7.5 J cm^{-3} and η of 85% improves on the prior ESP of roughly 400 kV cm^{-1}, broadening the application prospect.

SEM appearances of $x = 0.02$ and 0.08 ceramics in Fig. 6(a) and (b) are utilized as the matrix structure for a series of COMSOL simulations to validate the definite relationship
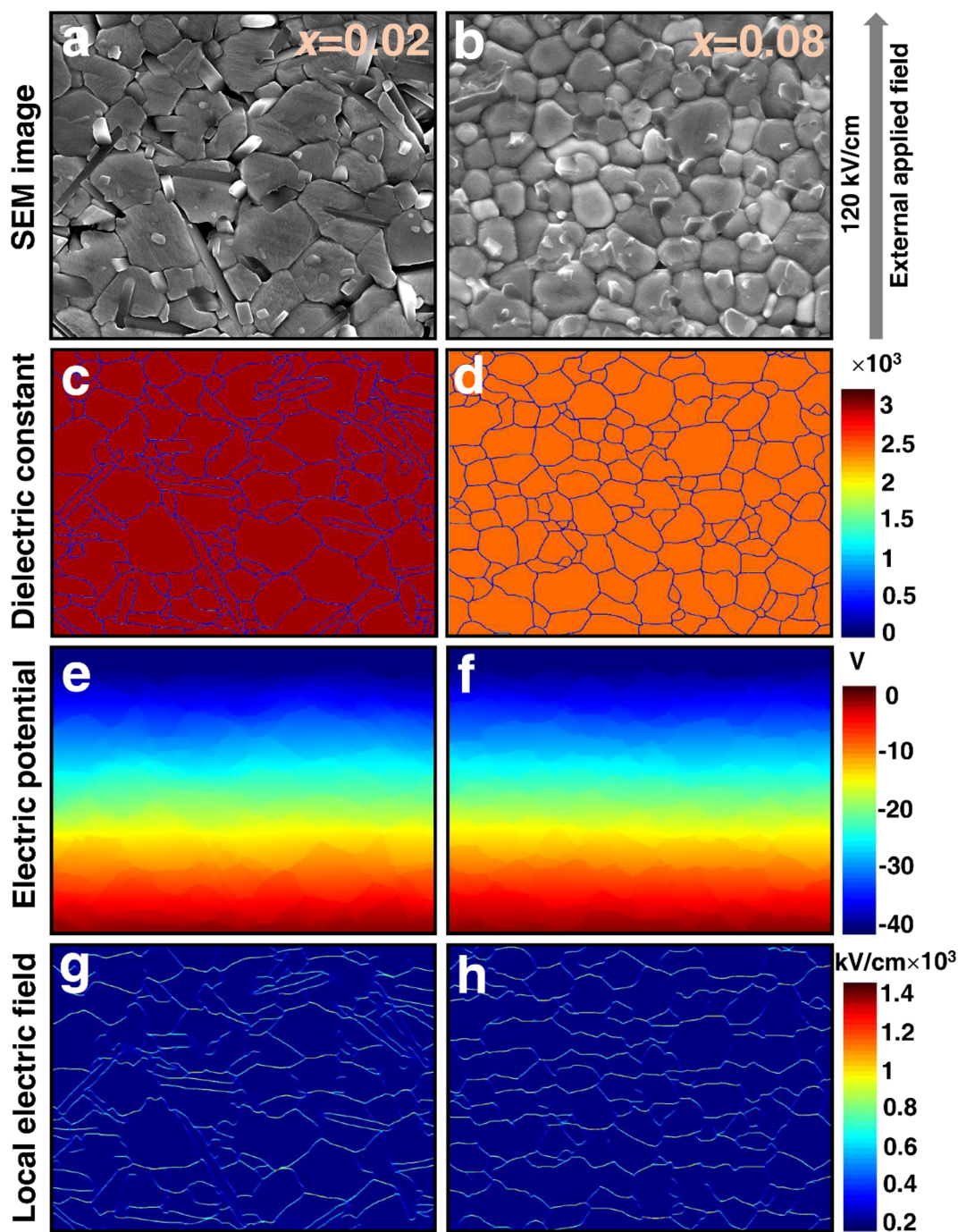

Fig. 6   The SEM of (a) $x = 0.02$ and (b) $x = 0.08$ ceramics as basic structures of the simulation. The ε_r distribution of (c) $x = 0.02$ and (d) $x = 0.08$ ceramics. The electric potential distribution of (e) $x = 0.02$ and (f) $x = 0.08$ ceramics. The local electric field distribution of (g) $x = 0.02$ and (h) $x = 0.08$ ceramics.
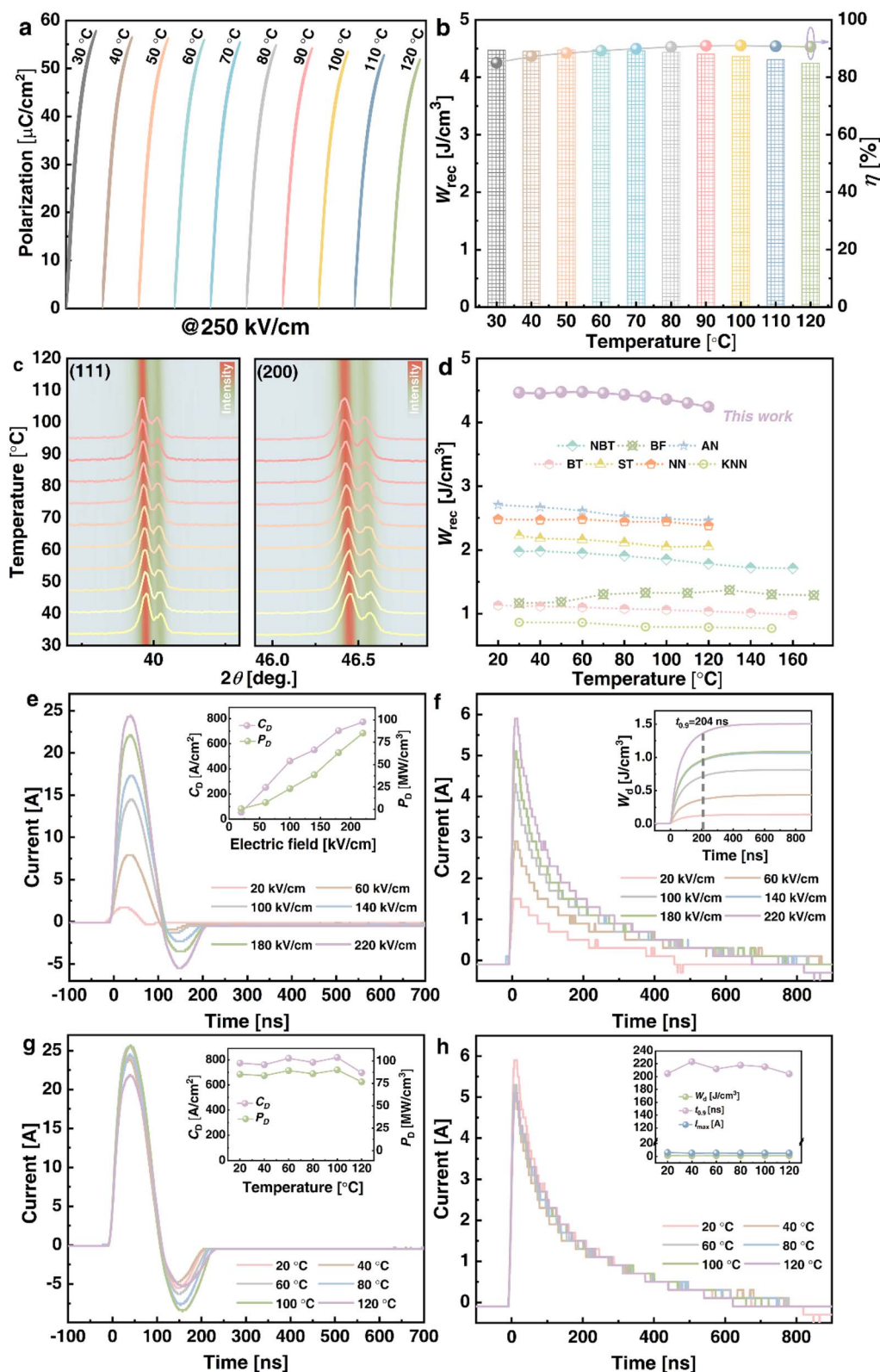
Fig. 7 (a) Unipolar $P–E$ loops (measured at 250 kV cm^{-1}) and (b) W_{rec} and η as functions of temperature for $x = 0.08$ (VPP) ceramics. (c) Temperature evolution of XRD patterns for $x = 0.08$ (VPP) ceramics from 30 °C to 120 °C at selected angles of 39.5–40.5° and 46–47°. (d) Comparison of W_{rec} at temperatures between this work and some recently reported lead-free ceramics. (e) Underdamped discharge and (f) overdamped discharge waveforms of the $x = 0.08$ (VPP) ceramic under various electric fields and ambient temperature. (g) Underdamped discharge and (h) overdamped discharge waveforms of the $x = 0.08$ (VPP) ceramic measured in the temperature range from 20 to 120 °C under 220 kV cm^{-1}.

2648 | J. Mater. Chem. A, 2023, 11, 2641–2651

This journal is © The Royal Society of Chemistry 2023

between microstructure and electrical properties. Because of the clear separation of grain boundaries and grains in these two ceramics, their own ε' of 3090 and 2469 at 1 kHz obtained from Fig. 3(b) and (d) are assigned as belonging to the grains, and the ε' of the grain boundaries is one-tenth of it. Following this setting, the model presented by Randall *et al.*[78] is used to simulate $x = 0.02$ and 0.08 ceramics, and the corresponding results are displayed in Fig. 6(c) and (d), respectively. Under a simulated external electric field of 120 kV cm^{-1} applied to $x = 0.02$ and 0.08 ceramics, the grain distributions of $x = 0.08$ are more uniform and denser than those of $x = 0.02$, resulting in a greater average electric potential, as shown in Fig. 6(e) and (f). Furthermore, when combined with the finer grains in $x = 0.08$ ceramics, Fig. 6(g) and (h) shows that $x = 0.08$ ceramics have more grain boundaries (shown in yellow) correlating to a strong local electric field, resulting in a higher E_b.

Aside from obtaining superior ESP at RT, its temperature adaptability throughout a broad temperature range is critical for energy storage applications. Fig. 7(a) and (b) exhibit the unipolar P–E loops and corresponding W_{rec} and η of $x = 0.08$ (VPP) ceramics from 30 to 120 °C at 250 kV cm^{-1}. Although P_m will certainly reduce slightly as temperature rises, the P–E loops will always remain slim, and P_r will likewise decrease. With the same changes in P_m and P_r, W_{rec} remains stable at 4.47 to 4.25 J cm^{-3} and the η rises from 85 to 91%. As a result, the combined W_{rec} of 4.4 J cm^{-3} and η of 89% with fluctuations of less than $\pm5\%$ and $\pm6\%$ indicate that stable thermal reactivity is attained in $x = 0.08$ (VPP) ceramics. Similarly, at 30–120 °C, the XRD patterns of the (111) and (200) peaks at 39.5–40.5° and 46–47° are shown in Fig. 7(c). The shape and intensity of the diffraction peak reflected by the background color essentially remain unchanged as the temperature changes. This structural evolution law can also be used to demonstrate the temperature independence of $x = 0.08$ (VPP) ceramics, which have superior ESP performance than other ceramic systems at various temperatures [see Fig. 7(d)].[15,36,66,74,79–81] In comparison to chosen NBT, BF, AN, BT, ST, NN, and KNN-based ceramics, $x = 0.08$ (VPP) ceramics stand out due to W_{rec} of 4.25 J cm^{-3} and η of 89%. Furthermore, the charge–discharge behaviors are critical for $x = 0.08$ (VPP) ceramics and are depicted in Fig. 7(e–h). The underdamped I–t curves from 20 to 220 kV cm^{-1} are displayed in Fig. 7(e). All curves perpendicularly increase as the electric field varies. Under 220 kV cm^{-1}, the maximum current (I_{max}), current density ($C_D = I_{max}/S$), and power density ($P_D = EI_{max}/2S$) are 24.5 A, 780.25 A cm^{-2} and 85.83 MW cm^{-3}, respectively. Fig. 7(f) shows the overdamped I–t curves in the same electric field range, while the corresponding discharged energy density ($W_d = R \int i^2 t \mathrm{d}t/V$, $R = 100 \, \Omega$)[82] is 1.51 J cm^{-3} and discharge time ($t_{0.9}$) is maintained within 204 ns. These two types of waveforms from 20 to 120 °C are also gathered in Fig. 7(g) and (h) for analyzing the temperature applicability of $x = 0.08$ (VPP) ceramics. Even if the waveforms and derived values change with temperature, its I_{max}, C_D, and P_D remain stable at 120 °C, which are 21.9 A, 697.45 A cm^{-2}, and 76.72 MW cm^{-3}, respectively, with a W_d of 1.26 J cm^{-3} and $t_{0.9}$ of 204 ns. As a result, $x = 0.08$ (VPP) ceramics exhibit superior thermal independence and competitiveness in energy storage and pulse performance.

4. Conclusions

To summarize, the stepwise optimization route is used to achieve comprehensive outstanding ESP in 0.65NBT-0.35BST-based ceramics by gradually introducing the BMS and implementing the VPP technique. Specifically, after generating a Sr^{2+}–Sr^{2+} ion pair at the A-site to assure a high P_m, the introduction of Mg^{2+} and Sn^{4+} ions at the B-site promotes PNRs and repeated rolling for ceramics increases compactness, which improve the ΔP and E_b in order. As a result, 0.92(0.65NBT-0.35BST)-0.08BMS-VPP ceramics obtain an ultrahigh W_{rec} of 7.5 J cm^{-3} and a high η of 85% under the action of a huge ΔP of 64.6 μC cm^{-2} at 440 kV cm^{-1}, as well as stable thermal reactivity within 20–120 °C. Such superior ESP benefits from the high polarization intensity, breaks the previous values at almost the breakdown electric field, and outperforms the majority of reported NBT-based ceramics, demonstrating the applicability of the stepwise optimization route for designing other similar high-performance dielectric ceramics.

Conflicts of interest

There are no conflicts to declare.

Acknowledgements

References

1 Z. Yang, H. Du, L. Jin and D. Poelman, *J. Mater. Chem. A*, 2021, **9**, 18026–18085.

2 L. Yang, X. Kong, F. Li, H. Hao, Z. Cheng, H. Liu, J. Li and S. Zhang, *Prog. Mater. Sci.*, 2019, **102**, 72–108.

3 B. Zhang, X. Chen, Z. Pan, P. Liu, M. Mao, K. Song, Z. Mao, R. Sun, D. Wang and S. Zhang, *Adv. Funct. Mater.*, 2022, **33**, 2210050.

This journal is © The Royal Society of Chemistry 2023

J. Mater. Chem. A, 2023, **11**, 2641–2651 | **2649**

4 J. Lv, Q. Li, Y. Li, M. Tang, D. Jin, Y. Yan, B. Fan, L. Jin and G. Liu, *Chem. Eng. J.*, 2021, **420**, 129900.

5 B. Guo, Y. Yan, M. Tang, Z. Wang, Y. Li, L. Zhang, H. Zhang, L. Jin and G. Liu, *Chem. Eng. J.*, 2021, **420**, 130475.

6 L. Jin, F. Li and S. Zhang, *J. Am. Ceram. Soc.*, 2014, **97**, 1–27.

7 J. Li, F. Li, Z. Xu and S. Zhang, *Adv. Mater.*, 2018, **30**, 1802155.

8 Z. Pan, D. Hu, Y. Zhang, J. Liu, B. Shen and J. Zhai, *J. Mater. Chem. C*, 2019, **7**, 4072–4078.

9 J. Li, Z. Shen, X. Chen, S. Yang, W. Zhou, M. Wang, L. Wang, Q. Kou, Y. Liu, Q. Li, Z. Xu, Y. Chang, S. Zhang and F. Li, *Nat. Mater.*, 2020, **19**, 999–1005.

10 F. Yan, K. Huang, T. Jiang, X. Zhou, Y. Shi, G. Ge, B. Shen and J. Zhai, *Energy Storage Mater.*, 2020, **30**, 392–400.

11 L. Zhang, S. Cao, Y. Li, R. Jing, Q. Hu, Y. Tian, R. Gu, J. Kang, D. O. Alikin, V. Y. Shur, X. Wei, G. Liu, F. Gao, H. Du, Y. Yan and L. Jin, *J. Alloys Compd.*, 2022, **896**, 163139.

12 Z. Sun, Z. Wang, Y. Tian, G. Wang, W. Wang, M. Yang, X. Wang, F. Zhang and Y. Pu, *Adv. Electron. Mater.*, 2020, **6**, 1900698.

13 L. Zhang, R. Jing, Y. Huang, Q. Hu, D. O. Alikin, V. Y. Shur, J. Gao, X. Wei, L. Zhang, G. Liu, Y. Yan and L. Jin, *J. Materiomics*, 2022, **8**, 527–536.

14 H. Li, S. Zhou, J. Zhao, T. Yan, Y. Du, H. Zhou, Y. Pu and D. Wang, *J. Adv. Dielectr.*, 2022, **12**, 2242007.

15 D. Hu, Z. Pan, X. Zhang, H. Ye, Z. He, M. Wang, S. Xing, J. Zhai, Q. Fu and J. Liu, *J. Mater. Chem. C*, 2020, **8**, 591–601.

16 Y. Wu, Y. Fan, N. Liu, P. Peng, M. Zhou, S. Yan, F. Cao, X. Dong and G. Wang, *J. Mater. Chem. C*, 2019, **7**, 6222–6230.

17 X. Zhang, D. Hu, Z. Pan, X. Lv, Z. He, F. Yang, P. Li, J. Liu and J. Zhai, *Chem. Eng. J.*, 2021, **406**, 126818.

18 X. Qiao, D. Wu, F. Zhang, B. Chen, X. Ren, P. Liang, H. Du, X. Chao and Z. Yang, *J. Mater. Chem. C*, 2019, **7**, 10514–10520.

19 Y. Tian, P. Song, G. Viola, J. Shi, J. Li, L. Jin, Q. Hu, Y. Xu, W. Ge, Z. Yan, D. Zhang, N. V. Tarakina, I. Abrahams, X. Wei and H. Yan, *J. Mater. Chem. A*, 2022, **10**, 14747–14787.

20 Y. Lin, D. Li, M. Zhang and H. Yang, *J. Mater. Chem. C*, 2020, **8**, 2258–2264.

21 D. Li, Y. Lin, Q. Yuan, M. Zhang, L. Ma and H. Yang, *J. Materiomics*, 2020, **6**, 743–750.

22 Z. Yang, F. Gao, H. Du, L. Jin, L. Yan, Q. Hu, Y. Yu, S. Qu, X. Wei, Z. Xu and Y. Wang, *Nano Energy*, 2019, **58**, 768–777.

23 D. Li, D. Zhou, D. Wang, W. Zhao, Y. Guo and Z. Shi, *Adv. Funct. Mater.*, 2022, **32**, 2111776.

24 F. Yan, H. Bai, Y. Shi, G. Ge, X. Zhou, J. Lin, B. Shen and J. Zhai, *Chem. Eng. J.*, 2021, **425**, 130669.

25 G. Liu, M. Tang, X. Hou, B. Guo, J. Lv, J. Dong, Y. Wang, Q. Li, K. Yu, Y. Yan and L. Jin, *Chem. Eng. J.*, 2021, **412**, 127555.

26 G. Liu, Y. Li, B. Guo, M. Tang, Q. Li, J. Dong, L. Yu, K. Yu, Y. Yan, D. Wang, L. Zhang, H. Zhang, Z. He and L. Jin, *Chem. Eng. J.*, 2020, **398**, 125625.

27 L. Jin, W. Luo, L. Wang, Y. Tian, Q. Hu, L. Hou, L. Zhang, X. Lu, H. Du, X. Wei, G. Liu and Y. Yan, *J. Eur. Ceram. Soc.*, 2019, **39**, 277–286.

28 Y. Pu, M. Yao, H. Liu and T. Frömling, *J. Eur. Ceram. Soc.*, 2016, **36**, 2461–2468.

29 W. Wang, L. Zhang, R. Jing, Q. Hu, D. O. Alikin, V. Ya. Shur, X. Wei, G. Liu, Y. Yan and L. Jin, *Chem. Eng. J.*, 2022, **434**, 134678.

30 Z. Yang, H. Du, L. Jin, Q. Hu, S. Qu, Z. Yang, Y. Yu, X. Wei and Z. Xu, *J. Eur. Ceram. Soc.*, 2019, **39**, 2899–2907.

31 Z. Yang, H. Du, L. Jin, Q. Hu, H. Wang, Y. Li, J. Wang, F. Gao and S. Qu, *J. Mater. Chem. A*, 2019, **7**, 27256–27266.

32 L. Zhang, R. Jing, Y. Huang, Q. Hu, D. O. Alikin, V. Y. Shur, D. Wang, X. Wei, L. Zhang, G. Liu and L. Jin, *J. Eur. Ceram. Soc.*, 2022, **42**, 944–953.

33 N. Luo, K. Han, F. Zhuo, C. Xu, G. Zhang, L. Liu, X. Chen, C. Hu, H. Zhou and Y. Wei, *J. Mater. Chem. A*, 2019, **7**, 14118–14128.

34 D. Wang, Z. Fan, D. Zhou, A. Khesro, S. Murakami, A. Feteira, Q. Zhao, X. Tan and I. M. Reaney, *J. Mater. Chem. A*, 2018, **6**, 4133–4144.

35 M. Zhou, R. Liang, Z. Zhou and X. Dong, *Ceram. Int.*, 2019, **45**, 3582–3590.

36 H. Yang, H. Qi and R. Zuo, *J. Eur. Ceram. Soc.*, 2019, **39**, 2673–2679.

37 W. Wang, Y. Pu, X. Guo, R. Shi, M. Yang and J. Li, *J. Alloys Compd.*, 2020, **817**, 152695.

38 X. Jiang, H. Hao, S. Zhang, J. Lv, M. Cao, Z. Yao and H. Liu, *J. Eur. Ceram. Soc.*, 2019, **39**, 1103–1109.

39 W. Wang, Y. Pu, X. Guo, R. Shi, Y. Shi, M. Yang, J. Li, X. Peng and Y. Li, *J. Eur. Ceram. Soc.*, 2019, **39**, 5236–5242.

40 W. Wang, Y. Pu, X. Guo, T. Ouyang, Y. Shi, M. Yang, J. Li, R. Shi and G. Liu, *Ceram. Int.*, 2019, **45**, 14684–14690.

41 Y. Pu, W. Wang, X. Guo, R. Shi, M. Yang and J. Li, *J. Mater. Chem. C*, 2019, **7**, 14384–14393.

42 M. Zhang, H. Yang, D. Li, L. Ma and Y. Lin, *J. Mater. Chem. C*, 2020, **8**, 8777–8785.

43 C. Xu, Z. Fu, Z. Liu, L. Wang, S. Yan, X. Chen, F. Cao, X. Dong and G. Wang, *ACS Sustainable Chem. Eng.*, 2018, **6**, 16151–16159.

44 H. Sun, X. Wang, Q. Sun, X. Zhang, Z. Ma, M. Guo, B. Sun, X. Zhu, Q. Liu and X. Lou, *J. Eur. Ceram. Soc.*, 2020, **40**, 2929–2935.

45 N. Luo, K. Han, L. Liu, B. Peng, X. Wang, C. Hu, H. Zhou, Q. Feng, X. Chen and Y. Wei, *J. Am. Ceram. Soc.*, 2019, **102**, 4640–4647.

46 B. Qu, H. Du and Z. Yang, *J. Mater. Chem. C*, 2016, **4**, 1795–1803.

47 F. Li, J. Zhai, B. Shen, H. Zeng, X. Jian and S. Lu, *J. Alloys Compd.*, 2019, **803**, 185–192.

48 N. Liu, R. Liang, X. Zhao, C. Xu, Z. Zhou and X. Dong, *J. Am. Ceram. Soc.*, 2018, **101**, 3259–3265.

49 Y. Tian, L. Jin, H. Zhang, Z. Xu, X. Wei, G. Viola, I. Abrahams and H. Yan, *J. Mater. Chem. A*, 2017, **5**, 17525–17531.

50 T. Shao, H. Du, H. Ma, S. Qu, J. Wang, J. Wang, X. Wei and Z. Xu, *J. Mater. Chem. A*, 2017, **5**, 554–563.

51 S. Li, H. Nie, G. Wang, C. Xu, N. Liu, M. Zhou, F. Cao and X. Dong, *J. Mater. Chem. C*, 2019, **7**, 1551–1560.

52 Z. Yang, H. Du, S. Qu, Y. Hou, H. Ma, J. Wang, J. Wang, X. Wei and Z. Xu, *J. Mater. Chem. A*, 2016, **4**, 13778–13785.

2650 | *J. Mater. Chem. A*, 2023, **11**, 2641–2651

This journal is © The Royal Society of Chemistry 2023

53 G. Wang, J. Li, X. Zhang, Z. Fan, F. Yang, A. Feteira, D. Zhou, D. C. Sinclair, T. Ma, X. Tan, D. Wang and I. M. Reaney, *Energy Environ. Sci.*, 2019, **12**, 582–588.

54 L. Yang, X. Kong, Z. Cheng and S. Zhang, *J. Mater. Chem. A*, 2019, **7**, 8573–8580.

55 Q. Hu, Y. Tian, Q. Zhu, J. Bian, L. Jin, H. Du, D. O. Alikin, V. Y. Shur, Y. Feng, Z. Xu and X. Wei, *Nano Energy*, 2020, **67**, 104264.

56 W. Wang, Y. Pu, X. Guo, R. Shi, M. Yang and J. Li, *Ceram. Int.*, 2020, **46**, 11484–11491.

57 N. Luo, K. Han, M. J. Cabral, X. Liao, S. Zhang, C. Liao, G. Zhang, X. Chen, Q. Feng, J. Li and Y. Wei, *Nat. Commun.*, 2020, **11**, 4824.

58 Z. Dai, J. Xie, W. Liu, X. Wang, L. Zhang, Z. Zhou, J. Li and X. Ren, *ACS Appl. Mater. Interfaces*, 2020, **12**, 30289–30296.

59 F. Si, B. Tang, Z. Fang, H. Li and S. Zhang, *Ceram. Int.*, 2019, **45**, 17580–17590.

60 B. Luo, X. Wang, E. Tian, H. Song, H. Wang and L. Li, *ACS Appl. Mater. Interfaces*, 2017, **9**, 19963–19972.

61 D. Li, D. Zhou, W. Liu, P. Wang, Y. Guo, X. Yao and H. Lin, *Chem. Eng. J.*, 2021, **419**, 129601.

62 L. Zhang, L. Pang, W. Li and D. Zhou, *J. Eur. Ceram. Soc.*, 2020, **40**, 3343–3347.

63 L. Zhao, Q. Liu, J. Gao, S. Zhang and J. Li, *Adv. Mater.*, 2017, **29**, 1701824.

64 Z. Lu, W. Bao, G. Wang, S.-K. Sun, L. Li, J. Li, H. Yang, H. Ji, A. Feteira, D. Li, F. Xu, A. K. Kleppe, D. Wang, S.-Y. Liu and I. M. Reaney, *Nano Energy*, 2021, **79**, 105423.

65 W. Li, D. Zhou, L. Pang, R. Xu and H. Guo, *J. Mater. Chem. A*, 2017, **5**, 19607–19612.

66 M. Zhou, R. Liang, Z. Zhou and X. Dong, *J. Mater. Chem. C*, 2018, **6**, 8528–8537.

67 H. Yang, Z. Lu, L. Li, W. Bao, H. Ji, J. Li, A. Feteira, F. Xu, Y. Zhang, H. Sun, Z. Huang, W. Lou, K. Song, S. Sun, G. Wang, D. Wang and I. M. Reaney, *ACS Appl. Mater. Interfaces*, 2020, **12**, 43942–43949.

68 J. Wu, A. Mahajan, L. Riekehr, H. Zhang, B. Yang, N. Meng, Z. Zhang and H. Yan, *Nano Energy*, 2018, **50**, 723–732.

69 X. Ren, L. Jin, Z. Peng, B. Chen, X. Qiao, D. Wu, G. Li, H. Du, Z. Yang and X. Chao, *Chem. Eng. J.*, 2020, **390**, 124566.

70 L. Zhao, J. Gao, Q. Liu, S. Zhang and J. Li, *ACS Appl. Mater. Interfaces*, 2018, **10**, 819–826.

71 F. Yan, X. Zhou, X. He, H. Bai, S. Wu, B. Shen and J. Zhai, *Nano Energy*, 2020, **75**, 105012.

72 X. Zhou, H. Qi, Z. Yan, G. Xue, H. Luo and D. Zhang, *ACS Appl. Mater. Interfaces*, 2019, **11**, 43107–43115.

73 W. Huang, Y. Chen, X. Li, G. Wang, N. Liu, S. Li, M. Zhou and X. Dong, *Appl. Phys. Lett.*, 2018, **113**, 203902.

74 Z. Dai, D. Li, Z. Zhou, S. Zhou, W. Liu, J. Liu, X. Wang and X. Ren, *Chem. Eng. J.*, 2022, **427**, 131959.

75 L. Zhu, X. Lei, L. Zhao, M. I. Hussain, G. Zhao and B. Zhang, *Ceram. Int.*, 2019, **45**, 20266–20275.

76 X. Gao, Y. Li, J. Chen, C. Yuan, M. Zeng, A. Zhang, X. Gao, X. Lu, Q. Li and J. Liu, *J. Eur. Ceram. Soc.*, 2019, **39**, 2331–2338.

77 M. Zhang, H. Yang, D. Li and Y. Lin, *J. Alloys Compd.*, 2020, **829**, 154565.

78 C. A. Randall, A. D. Hilton, D. J. Barber and T. R. Shrout, *J. Mater. Res.*, 1993, **8**, 880–884.

79 M. Zhou, R. Liang, Z. Zhou and X. Dong, *J. Mater. Chem. A*, 2018, **6**, 17896–17904.

80 S. Li, T. Hu, H. Nie, Z. Fu, C. Xu, F. Xu, G. Wang and X. Dong, *Energy Storage Mater.*, 2021, **34**, 417–426.

81 Y. Ding, P. Li, J. He, W. Que, W. Bai, P. Zheng, J. Zhang and J. Zhai, *Composites, Part B*, 2022, **230**, 109493.

82 L. Zhang, H. Sun, Y. Lan, M. Tang, Y. Li, D. O. Alikin, V. Y. Shur, J. Gao, X. Lu, X. Wei, Z. Xu and L. Jin, *Ceram. Int.*, 2022, **48**, 15711–15720.

This journal is © The Royal Society of Chemistry 2023

J. Mater. Chem. A, 2023, **11**, 2641–2651 | **2651**